



# Effect of Wrapping Force on the Effective Stiffness of Packed Parallel Wire Cables with Elastoplastic Contacts

Linda Teka<sup>1</sup>; Raimondo Betti, Ph.D., M.ASCE<sup>2</sup>; and Huiming Yin, Ph.D., M.ASCE<sup>3</sup>

**Abstract:** When cables use many wires packed in a hexagonal pattern wrapped by bands around the surface, effective stiffness plays an important role in structural integrity and safety. This paper studies cylindrical wires packed in a hexagonal lattice tightened up by wrapping bands. When a transverse load is applied, the stress transferred through the contacts between the wires can be represented by a center-center force network with the Hertz contact theory. When yielding is considered in the contact zone, an elastoplastic contact model is developed. The Singum model simulates the singular forces by the stress between continuum particles. The effective stress-strain relationship changes with the stress of the wrapping bands and exhibits isotropic behavior in the cross section. Therefore, the overall elastic behavior of the cable is transversely isotropic with a tailorable stiffness in the cross section by the wrapping force. This method is general for mechanical modeling of packed parallel wire cables, and its application to bridge cable testing and repair with development length prediction is underway. **DOI: 10.1061/JENMDT.EMENG-7731.** © 2024 American Society of Civil Engineers.

**Practical Applications:** This study introduces a novel approach, the Singum model, for analyzing the overall mechanical properties of packed wire cables, which are crucial for ensuring structural integrity and safety in various engineering applications. By investigating the effective transverse stiffness of packed wire cables through a combination of theoretical modeling, finite element analysis (FEM), and experimental tests, this research provides valuable insights into optimizing cable design and performance across diverse engineering applications such as cable domes, electric transmission lines, tramways, cable-stayed bridges, and suspension bridges. The findings highlight the significant impact of wrapping force on the effective stiffness of packed cylinders, offering engineers a means to tailor the stiffness of cable cross sections for specific requirements in these applications. This study provides a robust framework for advancing the understanding and optimization of packed wire cable systems in engineering practice with reasonable assumptions and simplifications, which can be tailored for specific materials or applications.

**Author keywords:** Contact mechanics; Wire cables; Hexagonal packing lattices; Singum model; Elastoplastic analysis; Transversely isotropic stiffness.

#### Introduction

Steel cables find extensive applications in engineering constructions, such as cable domes, electric transmission lines, tramways, cable-stayed bridges, and suspension bridges (Fig. 1), due to their exceptional capacity to provide effective structural solutions for achieving substantial spans. The primary cables within structural systems are of paramount importance as they bear critical loads, serving as essential structural components (Chacar 2001). Comprising thousands of parallel cylindrical steel wires, these cables

<sup>1</sup>Ph.D. Candidate, Dept. of Civil Engineering and Engineering Mechanics, Columbia Univ., 610 Seeley W. Mudd, 500 West 120th St., New York, NY 10027. ORCID: https://orcid.org/0009-0005-6074-7813. Email: lgt2115@columbia.edu

<sup>2</sup>Professor, Dept. of Civil Engineering and Engineering Mechanics, Columbia Univ., 610 Seeley W. Mudd, 500 West 120th St., New York, NY 10027. Email: betti@civil.columbia.edu

<sup>3</sup>Associate Professor, Dept. of Civil Engineering and Engineering Mechanics, Columbia Univ., 610 Seeley W. Mudd, 500 West 120th St., New York, NY 10027 (corresponding author). ORCID: https://orcid.org/0000-0001-6549-9066. Email: yin@civil.columbia.edu

Note. This manuscript was submitted on December 4, 2023; approved on May 7, 2024; published online on July 23, 2024. Discussion period open until December 23, 2024; separate discussions must be submitted for individual papers. This paper is part of the *Journal of Engineering Mechanics*, © ASCE, ISSN 0733-9399.

are encircled at intervals by wrapping bands [Fig. 1(c)]. The higher wrapping force leads to higher effective stiffness in the cross section, but the elastoplastic properties of steel may make mechanical behavior complex.

The contact mechanics among individual wires within these cables that are enveloped by wrapping bands have been the subject of prior investigation by scholars (Gjelsvik 1991; Raoof and Huang 1992). Many analytical, experimental, and numerical studies have been performed in the past in order to simulate and predict the contact properties (Hertz 1882; Radzimovsky 1953; Griffin 1961; Johnson 1987; Lankarani and Nikravesh 1989; Ghaednia et al. 2016; Olsson and Larsson 2016; Ghaednia et al. 2017), mainly the contact force, contact pressure, and indentations. However, most of these research studies are focused on elastic contact, and because of its complexity, no closed-form solution has been provided for elastoplastic contacts. In addition, most of the work focuses on spherical contacts, and only a few researchers have worked on cylindrical contacts (Sugunesh and Mertens 2021; Guo et al. 2020, 2022; Sharma and Jackson 2017). Despite a large amount of work existing on the contact of spherical elastic-plastic surfaces, little exists on the contact of cylinders in elastic-plastic contact. Therefore, the study of contacts, which include simultaneous elastic and plastic deformation in cylindrical contact, is crucial and applicable to real-life problems such as wire contacts and wheel contacts (Ghaednia et al. 2017).

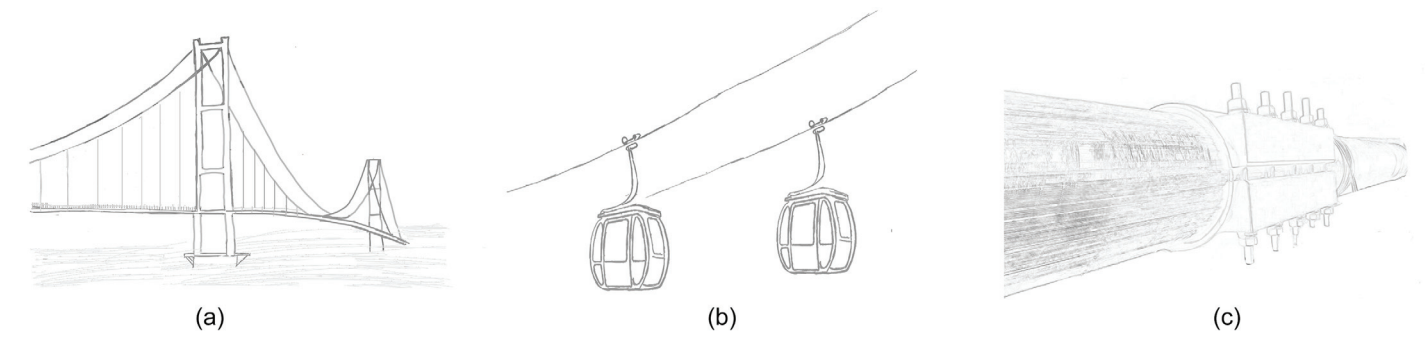


Fig. 1. Parallel wire cables: (a) cables in suspension bridges; (b) cables in electric cable cars; and (c) main cable wrapping clamps/bands.

In 1882, Hertz (1882) studied the normal force between two compressed elastic spheres. Hertz developed an expression for contact force with respect to the material properties and the radius of the spheres, which is used even now in most contact models. In 1985, Johnson (1987) developed a new model for cylindrical contacts that followed Hertzian contact theory. In addition, (Johnson 1987) considered plastic deformation in contact and showed that the restitution phase follows the Hertz theory even after yielding occurs. Johnson verified his results with Tabor's works (Tabor 2000) on the hardness of metals.

In literature, contact mechanics is divided into three phases: purely elastic, elastic-plastic, and fully plastic (Ghaednia et al. 2017). For a majority of metallic contacts, the elastic phase ends at very small deformations. The cylinders usually begin yielding at very small deformations, and the elastic regime only covers a small range of the deformation. The elastic-plastic regime initiates with the inception of yield and then transitions into the fully plastic regime. Many researchers have come up with analytical solutions for cylindrical contacts in the elastic phase (Radzimovsky 1953; Johnson 1987; Lankarani and Nikravesh 1989) based on the Hertz theory (Hertz 1882).

The contact between parallel wire cables mainly used in bridges has been defined using the Hertzian contact model (Hertz 1882) by researchers in the past (Gjelsvik 1991; Raoof and Huang 1992). When these cylindrical surfaces are loaded, the contact areas are extremely small, which results in high contact pressures and stresses. In many cases, this results in yielding in the contact regions, and thus, the elastic analysis is not accurate enough (Yin et al. 2023).

Ghaednia et al. (2017) reviewed over 200 published literature about the modeling of elastic-plastic contact and concluded that the average pressure during heavily loaded elastic-plastic contact is not governed by the conventional hardness to yield strength the ratio of approximately three but rather varies according to the boundary conditions and deformed geometry. Zhang et al. (2022) employed the finite element method (FEM) to investigate the behavior of an elastic-perfectly plastic hemisphere pressed by a rigid flat. The study defined the boundaries for regions of purely elastic, elastic-plastic, and fully plastic deformation and provided a new elastic-plastic constitutive model.

A continuum mechanics model proposed by Yin (2022) and Yin et al. (2023), the Singum model uses the Wigner–Seitz (WS) cells of a lattice to represent a continuum solid so that the singular point forces can be transformed into the contacting stress between the continuum particle. The elastoplastic constants can be obtained by applying a displacement variation from the relationship between the stress and the strain increments. This model can be used for the assembly of cylinders packed in a hexagon such as cable cars

[Fig. 1(b)] and bridge wire cables [Fig. 1(c)] and the relationship between the stiffness and the wrapping force can be formulated.

Finite element method (FEM) simulations have been widely used to predict the mechanical behavior of cable structures (Montoya et al. 2012; Brügger et al. 2022). However, FEM simulations often require significant computational resources and expertise, making them time-consuming and expensive. In contrast, the Singum model offers a computationally efficient alternative for predicting the stiffness of cable structures (Yin et al. 2023). By leveraging simplified analytical equations, this model provides accurate predictions while reducing computational costs and time requirements compared to FEM simulations.

In this study, the Singum model is presented as a method to analyze the mechanical characteristics of packed wire cables, where the cylindrical steel wires are arranged in hexagonal lattice structures. In this approach, an inner cylinder's behavior is emulated through a continuous Singum particle, while the interaction force between cylinders follows the Hertz contact model. This formulation allows for the determination of the effective constitutive relation of the cross section of the wire cables. Notably, variations in displacement give rise to configurational stresses caused by wrapping, consequently leading to a substantial alteration in the effective stiffness of the packed cylinders.

This paper studies the effective stiffness of packed wire cables employing the Singum model (Yin 2022; Yin et al. 2023), which is verified by the FEM and validated by the experimental tests. Firstly, the elastoplastic contact of two low-carbon steel cylinders is studied. The Hertz contact model (Johnson 1987) will be used to model the elastic relationship, and then initiation of plastic deformation is found analytically using the von Mises criterion (Green 2005). Experiments are conducted to validate the potential function. Secondly, cables containing cylindrical steel wires packed in a hexagonal lattice tightened up by wrapping bands at certain stress intervals are studied. By applying transverse load, the average material response is used to define the effective stiffness of the packed cylinder, which is homogenized by a transversely isotropic cylinder with a tailorable stiffness in the transverse plane. The effect of wrapping force on the effective transversal stiffness will be demonstrated. When one wire is broken, the force transfer among the neighboring wires will be very complex, which can be analyzed by the homogenized continuum containing a crack. The application of this theory to the development length of a broken wire in a cable is underway.

#### **Problem Statement**

When many wires are packed into a cable in a hexagonal pattern (Yin et al. 2023) in Fig. 2(a), they are commonly wrapped by

bands with a certain wrapping force, and the packed cable exhibits isotropic elastic behavior in the cross- while maintaining a high loading capacity in the axial direction. Although there exists space between circular wires, overall, the cable can be treated as a homogeneous cylinder with an effective stiffness

tensor **C** in Fig. 2(b). Yin et al. (2023) showed the cable is isotropic in the cross section. Therefore, the homogenized cylinder can be approximated as a transversely isotropic solid, and the stiffness tensor and its inverse can be written in the Voigt notation as

$$\mathbf{C} = \begin{pmatrix} C_{1111} & C_{1122} & C_{1133} & C_{1123} & C_{1131} & C_{1112} \\ C_{2211} & C_{2222} & C_{2233} & C_{2223} & C_{2231} & C_{2212} \\ C_{3311} & C_{3322} & C_{3333} & C_{3323} & C_{3331} & C_{3312} \\ C_{2311} & C_{2322} & C_{2333} & C_{2323} & C_{2331} & C_{2312} \\ C_{3111} & C_{3122} & C_{3133} & C_{3123} & C_{3131} & C_{3112} \\ C_{1211} & C_{1222} & C_{1233} & C_{1223} & C_{1231} & C_{1212} \end{pmatrix} = \begin{pmatrix} C_{11} & C_{12} & C_{13} & 0 & 0 & 0 \\ C_{12} & C_{11} & C_{13} & 0 & 0 & 0 \\ C_{13} & C_{13} & C_{33} & 0 & 0 & 0 \\ 0 & 0 & 0 & C_{44} & 0 & 0 \\ 0 & 0 & 0 & 0 & C_{44} & 0 \\ 0 & 0 & 0 & 0 & C_{44} & 0 \end{pmatrix}$$

$$(1)$$

and

$$\mathbf{C}^{-1} = \frac{1}{\Delta} \begin{pmatrix} C_{11}C_{33} - C_{13}^2 & C_{13}^2 - C_{12}C_{33} & (C_{12} - C_{11})C_{13} & 0 & 0 & 0 \\ C_{13}^2 - C_{12}C_{33} & C_{11}C_{33} - C_{13}^2 & (C_{12} - C_{11})C_{13} & 0 & 0 & 0 \\ (C_{12} - C_{11})C_{13} & (C_{12} - C_{11})C_{13} & C_{11}^2 - C_{12}^2 & 0 & 0 & 0 \\ 0 & 0 & 0 & \frac{\Delta}{C_{44}} & 0 & 0 \\ 0 & 0 & 0 & 0 & \frac{\Delta}{C_{44}} & 0 \end{pmatrix}$$

$$(2)$$

where 
$$\Delta = (C_{11}^2 - C_{12}^2)C_{33} - 2(C_{11} - C_{12})C_{13}^2$$
.

The five independent elastic constants are correlated with the tensor-form components as  $C_{11} = C_{1111}$ ,  $C_{12} = C_{1122}$ ,  $C_{13} = C_{1133}$ ,  $C_{33} = C_{3333}$ , and  $C_{44} = C_{1313}$ . Engineering strain shall be used with the Voigt notation, whereas the present strain tensor follows the tensor-form notation.

For a long cable, there is a high risk that a wire may be broken inside the cable, and how the load in the wire is transferred to the neighboring cables is a very challenging task for structural analysis and modeling. Because the contact area between wires increases with the wrapping force, the longitudinal force transfer will be affected by the wrapping force as well. If the effective stiffness of the homogenized cylinder in Fig. 2(b) is given, the broken wire can be simulated as a hexagonal-shaped crack in the transversely isotropic solid, which can provide insight into the force transfer from the broken wire to other wires. Therefore, the correlation between the transversely isotropic tensor C and the cable configuration, including material constants and wrapping force, will be critical for the stress transfer of cables with wire head-tail connections (Gjelsvik 1991).

In this paper, the material properties of the steel wires purchased from McMaster-Carr Supply Company with Part Number 8920K48 considered are shown in Table 1. To formulate the problem, the following assumptions are used:

- 1. The deformation in the wires is elastic-perfectly plastic;
- The wires interact through the Hertz contact model with small contact areas;

- 3. The wires can roll, but no slip occurs in the axial direction;
- 4. The yielding zone is localized in the neighborhood of the small contact areas, and the effect of permanent deformation on the wire is disregarded so that the wire's overall deformation is still linear elastic during the service.

In our analysis, we will begin by examining the elastic behavior within the cross section. Based on Assumption 3, despite the presence of shear forces along the axial direction, the cross section experiences only normal stress, resulting in interaction forces between the wires being directed along the center-center line. When unloading is considered, in the context of Assumption 4, one can superimpose an elastic analysis onto the existing solution for classic elastoplastic analysis, which leads to permanent deformation or residual stresses. However, for simplicity, this paper does not consider material and geometric changes resulting from the cyclic load's residual stress and permanent deformation due to the small contact area. In the actual applications, Assumptions 3 and 4 can be released with specific constitutive modeling parameters.

Therefore, with the increase of wrapping force, the contact deformation is divided into two stages: (1) the elastic state for the whole domain and (2) the elastoplastic stage with a yielding zone. The elastic perfectly plastic model is used for steel wire. Our previous paper (Yin et al. 2023) has studied the first stage, which will be reviewed in the next section, while the second stage will be studied with the FEM analysis to generate the loading curve.

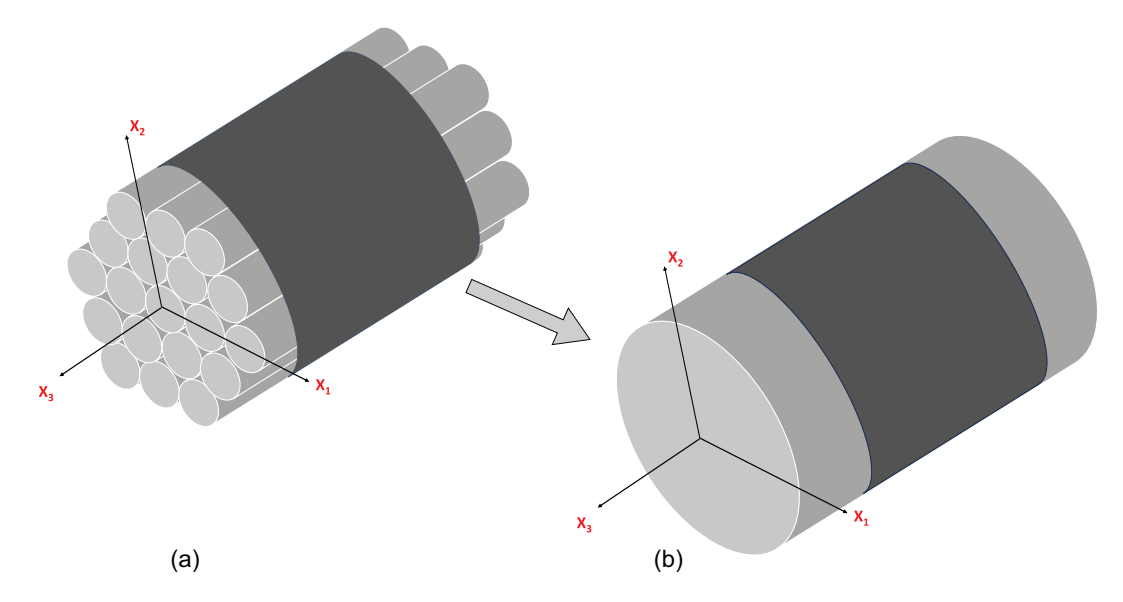


Fig. 2. Homogenization of packed wires into a uniform cylinder: (a) wire cable with a wrapping band; and (b) a homogenized cylinder with an effective transversely isotropic stiffness tensor.

**Table 1.** Mechanical properties of steel wires

Property	Value
Material	Low carbon steel
Diameter 2R (mm)	50
Poisson's ratio $\nu$	0.3
Elastic modulus $E$ (MPa)	200,000
Yield strength $\sigma_y$ (MPa)	413.6

Along the axial direction, the effective area ratio of wire in the cross section of a hexagonal lattice is

$$\phi = \frac{\sqrt{3}\pi}{6} \approx 0.9069 \tag{3}$$

Given a uniaxial test loading  $\sigma_{33}$  along  $x_3$  or a simple shearing  $\sigma_{31}$  or  $\sigma_{32}$  in  $x_1-x_3$  or  $x_2-x_3$  plane, because the force is uniformly transferred in the cross section of the cable, the effective Young's modulus and shear modulus will be factored by  $\phi$  and the Poisson's ratio will remain the same with the affine transformation. Therefore, one can obtain

$$\begin{split} \frac{\Delta}{C_{11}^2-C_{12}^2} &= C_{33} - \frac{2C_{13}^2}{C_{11}+C_{12}} = \phi E; \\ \frac{(C_{11}-C_{12})C_{13}}{C_{11}^2-C_{12}^2} &= \frac{C_{13}}{C_{11}+C_{12}} = \nu; \qquad C_{44} = \phi \frac{E}{2(1+\nu)} \end{split} \tag{4}$$

If the stiffness in the cross section is obtained with two material constants, we can predict the overall transversely isotropic stiffness in the 3D space with the previous three elastic constants. Note that the major and minor symmetry of the effective stiffness depends on the nonslip condition and equilibrium of the wires (Yin and Liu 2023).

In the cross section, due to the large stress variation at the contacts, elastoplastic deformation should be considered. In the following, we will begin by deriving the elasto-plastic contact of cylinders. Following this, the singum model will be introduced for the constitutive modeling.

This paper specifically addresses the characteristics of general cables subjected to a uniform wrapping force. In a wire cable of Fig. 1(c), the wrapping force is applied to the wires through bands with a width of 91.4.cm (approximately 3 ft) and an interval of 6 m (20 ft). It is crucial to note that the analysis presented herein is confined to the section encompassed by these bands, and any stress analysis beyond this area falls outside the purview of this paper. The current investigation lays the foundation for a subsequent study on high-strength wires of bridge cable, a study that is currently underway.

#### **Elastoplastic Contact of Cylinders**

Most works on cylinder contact have focused on the elastic relationship (Johnson 1987; Lankarani and Nikravesh 1989, 1994; Goldsmith 1999; Radzimovsky 1953), only a few researchers have accounted for the elastic-plastic behavior of the contact area by using the FEM method and approximations (Dumas and Baronet 1971; Komvopoulos 1989; Guo et al. 2020; Cinar and Sinclair 1986; Sharma and Jackson 2017). In the following, a combination of FEM and Johnson's elasticity theory for two cylinders in contact (Johnson 1987) are used to find analytical solutions for the elastoplastic contact of cylinders. The elastic stage of the contact is found analytically using Johnson's formula (Johnson 1987), which correlates contact load, contact half width, and deformation (interference) within the elastic range until plastic deformation begins. The initiation of plastic deformation is found analytically by using the existing formulation that was based on the von Mises yield criterion (Green 2005). An FEM analysis is performed to find the relationship between load and interference. Finally, the equations are validated against experimental results, which will be elaborated in the subsequent sections.

#### Elastic Contact Stage

In the context of cylindrical contact scenarios, two predominant mechanical states are commonly considered to simplify the three-dimensional (3D) configuration by a two-dimensional (2D) problem: plane strain and plane stress (Cinar and Sinclair 1986;

Johnson 1987; Ghaednia et al. 2017). Plane strain is often applicable when the cylindrical ends are rigidly held, leading to negligible strain beyond the cross sectional plane perpendicular to the cylinder's axis of symmetry. Conversely, lubricated cylinders that lack end restraints exhibit characteristics akin to the plane stress state due to the absence of end confinement, resulting in limited stress propagation outside the plane perpendicular to the cylinder's axis of symmetry. Ghaednia et al. (2017) argues that even when significant friction is introduced, the interaction between identical cylinders in contact does not result in relative motion. Consequently, the contact of unconstrained identical cylinders leans toward the plane stress state. However, mathematically, plane strain and plane stress can share the same form of formulation by replacing Young's modulus and Poisson's ratio (Yin and Zhao 2016). Following Johnson (1987), we can define the effective elastic modulus  $E^*$  as

$$E^* = \frac{E}{2(1-\nu^2)}$$
 and  $\frac{E}{2}$  (5)

for plane strain or plane stress, respectively.

When two identical cylinders with un-deformed radius R are compressed by a given load  $P_e$  per unit length, the relationship between the interference  $\delta_e$  and the force  $P_e$  is given by Yin et al. (2023) as

$$\delta_e = \frac{P_e}{\pi E^*} \left( \ln \frac{8\pi E^* R}{P_e} - 1 \right) \tag{6}$$

Note that in the literature,  $R^*$  is used in place of R in this paper, which leads to a difference of the coefficient of 2. Defining the change in center-center distance in this elastic range as  $\lambda_e = 1 - (\delta_e/2R)$ , which is also called the stretch ratio of the centercenter bond. Hence, we can rewrite Eq. (6) as:

$$\lambda_e = 1 - \frac{P_e}{2\pi E^* R} \left( \ln \frac{8\pi E^* R}{P_e} - 1 \right) \tag{7}$$

Although the force-interference  $(P-\lambda)$  equation Johnson (1987) has been implicitly given in the previous equation, by using the Lambert W function, denoted as W(z), which is the inverse function of  $z=We^W$ , the force can be written in term of  $\lambda_e$  as follows:

$$P_{e} = -\frac{\pi \delta_{e} E^{*}}{W_{-1} \left[ \frac{-e \delta_{e}}{8R} \right]} = \frac{2\pi E^{*} R(\lambda_{e} - 1)}{W_{-1} [0.25 e(\lambda_{e} - 1)]}$$
(8)

where  $W_{-1}(z)$  function is the second branch of Lambert W function with  $z=0.25e(\lambda_e-1)$ . Note that for the linear elastic contact problem, we can write -1/e < z < 0. In this range, there exist two branches of the W function. When  $z \to 0$ , the main branch of  $W(z) \to 0$ ; whereas the second branch of  $W_{-1}(z) \to -\infty$ . Here the second branch shall be applied, because when  $\lambda_e \to 1$ ,  $W_{-1}[0.25e(\lambda_e-1)] \to -\infty$  to make  $P_e \to 0$ . Herein, the subscript of -1 in  $W_{-1}$  is to differentiate it from the main branch. Its derivative can be written as  $(dW_{-1}/dz) = \{W_{-1}(z)/z[1+W_{-1}(z)]\}$ , which is applicable to both branches.

Fig. 3 shows the comparison between Johnson (1987)'s contact model, experimental test, and FEM results for the elastic contact of cylinders. It can be seen that the analytical formulation is a good fit for the FEM results with 3% error. The experiment results are close to the plane strain assumption with an error of 5% compared with the FEM and analytical results.

The experimental testing configuration and procedure have been introduced in Appendix I. With the increase of  $\delta_e$ , the difference between the modeling and testing results increases as well because of the elasto-plastic behavior of the low-carbon steel.

## Elastoplastic Contact Stage

Green (2005) expressed the critical mean contact pressure at which yielding of the contact model starts by using the von Mises stress criteria and Hertz (1882) stress state, which provides the interference  $\delta_c$  and the force per unit length  $P_c$  at the initiation of yielding as

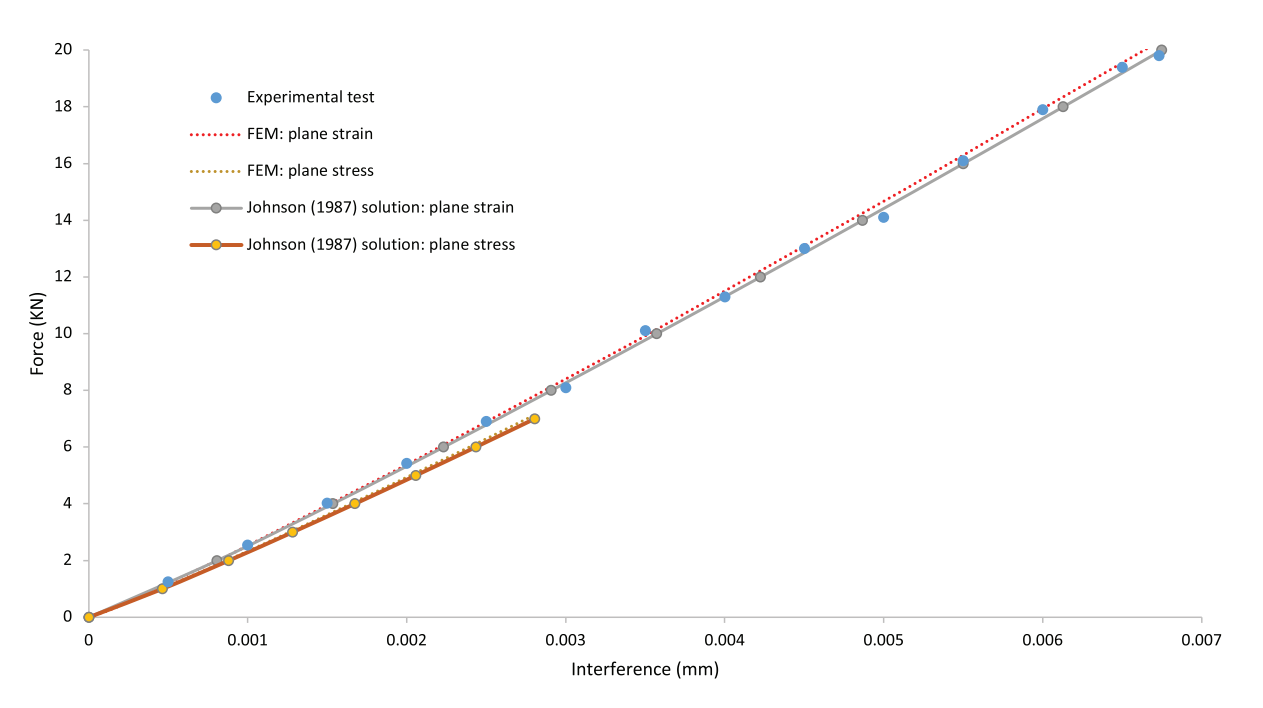


Fig. 3. Elastic contact of two cylinders in plane stress and plane strain assumptions for 100 mm long cylinders: Johnson (1987) analytical solution compared to the FEM and experimental results.

$$\delta_c = \frac{R}{2} \left( \frac{C\sigma_y}{E^*} \right)^2 \left( 2 \ln \frac{4E^*}{C\sigma_y} - 1 \right) \tag{9}$$

and

$$P_c = \frac{\pi R (C\sigma_y)^2}{2E^*} \tag{10}$$

where  $\sigma_y$  the maximum von Mises stress and C is a constant value that depends on Poisson's ratio, and it is given by Green (2005) as (1) for the plane stress condition, C = 1, and (2) for the plane strain condition

$$C = \begin{cases} \frac{1}{\sqrt{1 + 4(\nu - 1)\nu}} & \nu \le 0.1938\\ 1.164 + 2.975\nu - 2.906\nu^2 & \nu > 0.1938 \end{cases}$$
(11)

where  $\nu$  is the Poisson's ratio. The derivation of  $P_c$ ,  $\delta_c$ , and C is reviewed in Appendix II (Green 2005), which exhibits a minor difference of  $\delta_c$  from the original solution of Green (2005).

The critical stretch ratio at the initiation of yielding can be written as

$$\lambda_c = 1 - \frac{1}{4} \left( \frac{C\sigma_y}{E^*} \right)^2 \left( 2 \ln \frac{4E^*}{C\sigma_y} - 1 \right) \tag{12}$$

For example, the low carbon steel wires in Table 1 exhibit the corresponding parameters shown in Table 2 (Green 2005).

As the normal load P increases, the contact exceeds the initial yield point interference  $\delta_c$ . The elastoplastic phase is the stage after the initiation of yield,  $\delta_c$ , and before fully plastic with interference  $\delta_p$ . Therefore, the elastoplastic interference  $\delta_{ep}$  is in the range of  $\delta_c < \delta_{ep} < \delta_p$ , in which  $\delta_p$  is the critical displacement of the cylinder to reach the fully plastic stage, at which no additional load can be sustained.

During the elastoplastic stage, since both elastic and plastic deformations occur, it is impossible to obtain an analytical solution

**Table 2.** Yielding parameters for low carbon steel wires in Table 1

2D assumption	С	$\delta_c$ (m)	$\lambda_c$	$P_c$ (kN/m)
Plane strain	1.795	$6.7134 \times 10^{-6}$	0.99986	196.96
Plane stress	1	$2.726 \times 10^{-6}$	0.999945	67.177

(Guo et al. 2020, 2022). Subsequently, we will assume that the contact will be in the plastic stage after the initial yielding. In this study, we will only assume two stages: the elastic stage and the plastic stage. FEM analysis is conducted to study the elastic-plastic contact mechanics of two cylinders, and an explicit relation between the interference and the contact force will be formulated subsequently in the next section.

As the force pressing the cylinder continues to increase, the yielding zone in the material increases. Eventually, the cylinders may exhibit the complete plastic deformation stage, in which the average contact pressure is close to the yield strength. Some researchers have performed FEM of cylindrical contacts with flat surfaces (Dumas and Baronet 1971; Sharma and Jackson 2017; Cinar and Sinclair 1986), and particularly Cinar and Sinclair (1986) found that the pressure in the plastic range for cylindrical contacts in plane strain was approximately  $2.24\sigma_{\nu}$ .

The next section aims to fill a gap in the existing knowledge by developing empirical relationships for elastic, perfectly plastic cylindrical contacts under both plane strain and plane stress conditions. This is important because while there are models for elastic contacts (Johnson 1987) and some insight into plastic deformation initiation (Green 2005), currently, there is a lack of comprehensive models for situations where both elastic and plastic deformations occur in cylindrical contacts under the plane strain assumption.

### Numerical Analysis of Cylindrical Contacts

ABAQUS is used as a tool to perform the FEM analysis of the contact between two frictionless elastic–plastic cylindrical bodies. A symmetrical cylindrical model was used for a faster converging analysis. Normal surface-to-surface interaction is used to define the contact property, and since the cylinders are assumed to be frictionless, the tangential interaction was set to frictionless. The analysis is done under static loading conditions.

Finer mesh is used near the contact area, and relatively larger meshes were used for the rest of the model to reduce the computational time, as seen in Fig. 4. The symmetry of the cylinders was taken into account for the modeling, and the nodes at the bottom of the bottom cylinder were fully restrained, and only horizontal translation was constrained for the top cylinder. A static load was applied to the top cylinder. The total number of elements used for the analysis is 180,514, of which 175,040 is a linear quadrilateral element of type CPE4R and 5,474 are linear triangle elements of type CPE3 for the plane strain model. For the plane stress model, 140,494 linear quadrilateral elements of type CPS4R and 4,446

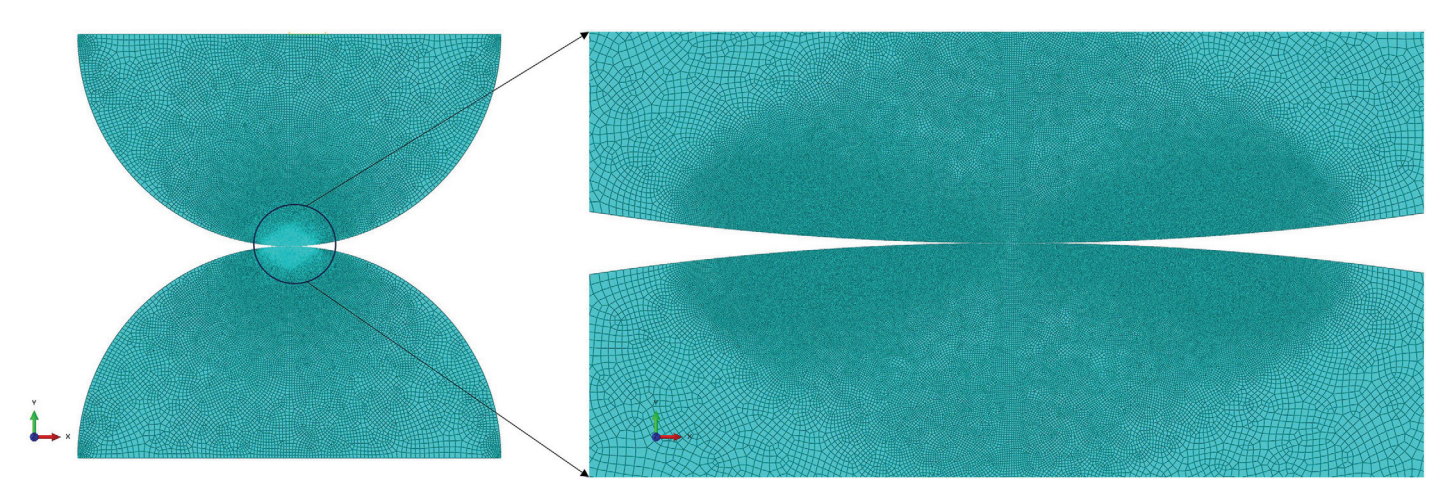


Fig. 4. Meshed FEM model of two cylinders in contact.

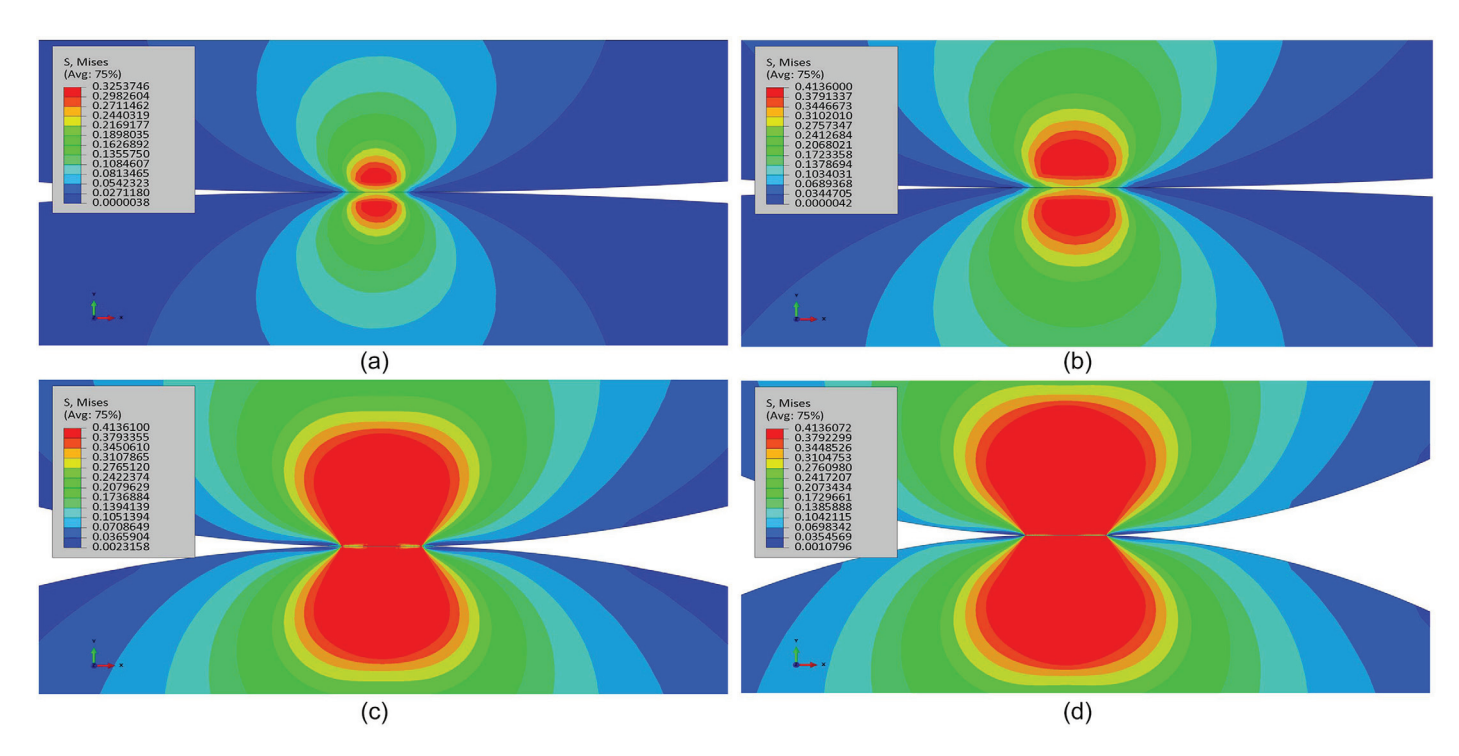


Fig. 5. The von Mises stress distributions for cylindrical contact in plane strain, GPa: (a)  $\delta = 0.004$  mm; (b)  $\delta_c = 0.0067$  mm; (c)  $\delta = 0.05$  mm; and (d)  $\delta = 0.1$  mm.

linear triangle elements of type CPS3 are used, totaling 144,940 elements and 143,622 nodes.

The von Mises stress distribution results from the FEM analysis are shown in Figs. 5 and 6 for plane strain and plane stress, respectively.

As anticipated, the rise in stress aligns with the increase in deflection. The cylinders are assumed to possess elastic-perfectly

plastic behavior, resulting in the maximum von Mises stress equating to the cylinder's yield strength of 413.6 MPa. Upon comparing the diagrams of plane strain depicted in Fig. 5 with the assumptions of plane stress shown in Fig. 6, a noteworthy distinction emerges. Taking a closer examination of the stress contours at the onset of yielding, where the interference equals  $\delta_c$ , as depicted in Figs. 5(b) and 6(a) for plane strain and plane stress, respectively, reveals

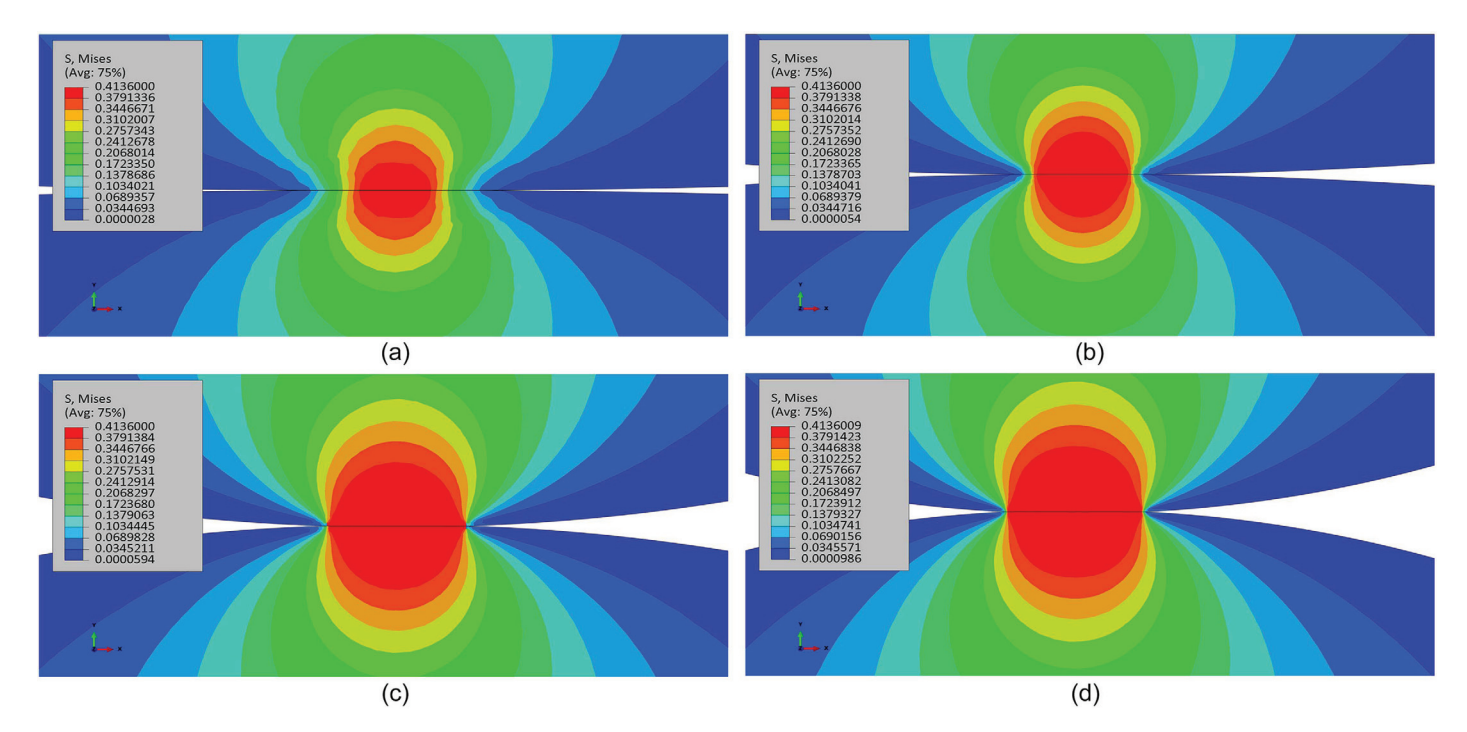


Fig. 6. von Mises stress distributions for cylindrical contact in plane stress, GPa: (a)  $\delta_c = 0.0027$  mm; (b)  $\delta = 0.01$  mm; (c)  $\delta = 0.05$  mm; and (d)  $\delta = 0.1$  mm.

distinct patterns in the evolution of plastic region formation. As the stresses increase, yielding initiates at the point of maximum von Mises stress (Jackson and Green 2005; Kogut and Etsion 2002). Under the plane strain assumption, as illustrated in Fig. 5(b), yielding commences below the contact surface, while under plane stress, as demonstrated in Fig. 6(a), yielding initiates on the contact area. In the case of plane strain, an elastic enclave materializes, following the concept introduced by Cinar and Sinclair (1986). The onset of plastic deformation initiates beneath the surface and advances with the increasing load. This enclave of elastic material takes the shape of an inside circle as the material undergoing plastic deformation encircles a central portion of the contact surface. With increasing interference, the plastic region expands until it reaches the surface of the cylinder, as shown in Fig. 5(d).

The range of deformation depicted in Figs. 5(b) and 6(a) underscores the absence of this elastic material enclave for cylindrical contacts subjected to plane stress conditions. The occurrence of this enclave in plane strain configurations is attributed to the prevalence of hydrostatic stress in the vicinity just beneath the central point of contact(Cinar and Sinclair 1986; Sharma and Jackson 2017). Achieving a hydrostatic stress state necessitates equality among the principal stresses in all three dimensions. In contrast, for the plane stress scenario, one direction of strain lacks constraints, resulting in zero stress along that axis. Consequently, hydrostatic stress cannot manifest, and the elastic enclave does not manifest in stress distributions for plane stress scenarios involving cylindrical contacts. Additionally, this variance dictates that the point of initial yielding in plane stress scenarios consistently transpires on the surface rather than below it, as elucidated by Cinar and Sinclair (1986), Green (2005), and Sharma and Jackson (2017).

Sharma and Jackson (2017) studied the elastoplastic contact of cylinders against rigid plates with bilinear hardening in plane stress conditions and gave an empirical relationship for the contact width as a function of displacement and force by fitting FEM results as follows:

$$\left(\frac{P}{P_c}\right)^{0.463} = 7.1 \left(\frac{E^*}{\sigma_v}\right)^{0.01} \left[\left(\frac{\delta}{\delta_c}\right)^{0.1} - 1\right] + 1 \tag{13}$$

which is given for  $\sigma_y/E = 0.002$ . Eq. (13) is for plane stress assumption, and for parallel wire cables used in aerial tramways, transmission lines, and bridges, a plane strain assumption is better

fitted since these structures span for very long distances. Although this concise equation can fit the FEM results very well and exhibit continuity with for the  $P-\delta$  curve at  $\delta_c$ , the derivative of  $P_{,\delta}$  is discontinuous. Actually, because the yielding zone continuously increases from one point to an area (Fig. 5) at  $\lambda=\lambda_c$ ,  $P_{,\lambda}$  shall continuously change with  $\lambda$  as well. This is different from the uniaxial loading of a specimen with a uniform cross section, where the slope of the load-displacement curve exhibits a discontinuity because the cross-sectional area reaches the yield point at the same time. The smooth continuity can be observed in Fig. 7 or the curves shown in Sharma and Jackson (2017).

With the elastoplastic contact loading curve rendered by the FEM in Fig. 7, we can use a polynomial function to fit the  $P-\lambda$  curve as follows:

- 1. Determine C,  $\lambda_c$ , and  $P_c$  from Eqs. (9)–(12).
- 2. Calculate the derivative of  $k_1 = (dP/d\lambda)$  at  $\lambda_c$ .
- 3. Fit the FEM results for the data with  $P > P_c$  by the function of  $P = P_c + \sum_{i=1}^{N} k_i (\lambda \lambda_c)^i$ . Here depending on the required accuracy, we can use three terms to obtain good accuracy with  $k_2$  and  $k_3$  to be determined by curve fitting.
- 4. Evaluate the deviation of the curve from the fitting function.

The contact force-displacement diagram for the plastic FEM analysis of two cylinders in plane strain is shown in Fig. 7(a) along with the fitted curves with the polynomial with N=2, 3, and 4, in which N=4 provides the best fitting and is used for the following analysis. Fig. 7(b) shows the  $P-\lambda$  curve of the elastic and perfectly plastic contact of two cylinders with the analytical function of N=4 as follows:

$$P = \begin{cases} \frac{2\pi E^* R(1-\lambda)}{W_{-1}[0.25e(1-\lambda)]} & \lambda_c < \lambda < 1\\ P_c + \sum_{i=1}^N k_i (\lambda - \lambda_c)^i & \lambda_p \le \lambda \le \lambda_c \end{cases}$$
(14)

where  $P_c = 0.19697E6$  (N/m) and  $\lambda_c = 0.99987$  are provided in Table 2, and  $k_i$  ( $i = 1, 2, \ldots, N$ ) are obtained by the curve fitting with tailorable accuracy by the number N of the polynomial order shown in Table 3 for three cases of N = 2, 3, 4. Here,  $\lambda_p$  indicates the limit of the elastoplastic deformation with the maximum contact force. As shown in Fig. 7(b),  $\lambda_p$  is obtained when the slope of the curve reaches zero. It shall be much higher than the range in this figure. Because this paper assumes that the contact area is very small,  $\lambda_p$  is far beyond the practical application of cables.

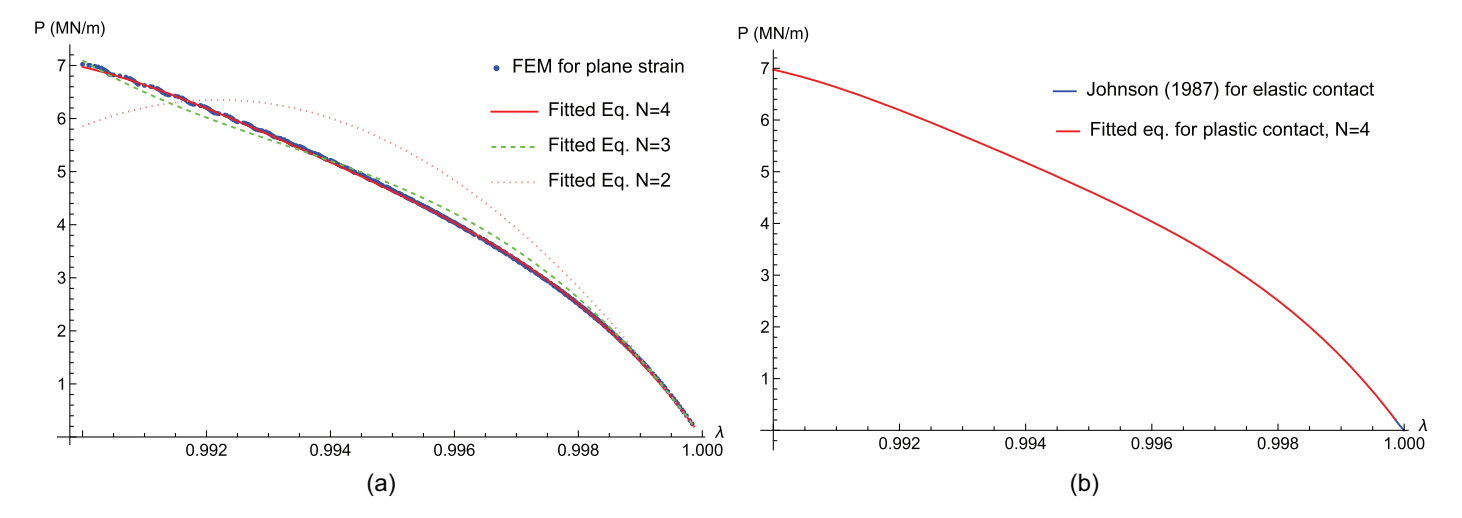


Fig. 7. Elastoplastic contact modeling: (a) contact force versus interference (displacement) of two cylinders in plane strain; and (b) the  $P-\lambda$  relationship for elastoplastic contact of two cylinders.

**Table 3.** The function of  $P(\lambda)$  for the elastoplastic contact by curve fitting with a polynomial function with N=2,3,4

$P(\lambda)$	$k_1$ (N/m)	$k_2  (\mathrm{N/m})$	k <sub>3</sub> (N/m)	k <sub>4</sub> (N/m)	Error (%)
N=2	$-1.60314 \times 10^9$	-104.393	NA	NA	21
N=3	$-1.60314 \times 10^9$	-180.863	-9,044.28	NA	6.13
N = 4	$-1.60314 \times 10^9$	$-236.077 \times 10^9$	$-23,916.1 \times 10^9$	$-952,955 \times 10^9$	1.07

Therefore, the mechanical behavior at this load limit is beyond the scope of this paper. As a default range of  $\lambda \in (\lambda_p, 1)$ ,  $\lambda_c$  is a critical point to divide the material behavior into elastic and elastoplastic ranges. In the following,  $\lambda$  is compared with  $\lambda_c$  only. Small N, say N=2 or 3, can provide a decent accuracy when the load limit is not too far from  $\lambda_c$ . When the plastic load is as high as P=6 MN/m, the case of N=4 matches the FEM results with an error of 1% in Fig. 7(a). At the neighborhood of  $\lambda_c$ ,  $P(\lambda)$  is continuous up to the first derivative as shown in Fig. 7(a) for three cases of N in comparison with the Hertzian model (Johnson 1987).

Note that the curve fitting is conducted for low-carbon steel wires under an elastic and perfectly plastic assumption. For high-strength wires, the previous procedure can be generalized to a new form of  $P(\lambda)$  in the elastoplastic range. Because of the smooth continuity of the elastoplastic contact and a small range for allowable elastoplastic deformation in the high-strength wire, a few polynomial terms (N=2 or 3) can provide a good fitting to the curve.

#### Effective Stiffness of a Packed Cable

When many parallel wires are packed into a cable with wrapping bands, the cable becomes an integrated structural member with a certain stiffness and strength. This section aims at the prediction of the stiffness of a packed cable with a certain wrapping force. In the longitudinal direction, the stiffness has been provided in Eq. (4). Therefore, we will focus on the stiffness in the  $x_1-x_2$  plane. Based on the recent work (Yin et al. 2023), when the wires are packed in a hexagonal lattice, the effective elasticity is isotropic in the cross section. Therefore, when  $C_{1,111}$  and  $C_{1,122}$  are derived, the full transversely isotropic stiffness tensor can be obtained.

# The Singum Model for Stiffness in the Cross Section of the Cable

Yin (2022) introduced the Singum model, which aims to establish a connection between pairwise interactions between nodes of a lattice structure and the effective elastic properties of solids. The cross section of cable can be represented by a hexagonal lattice, in which the wire's center-center connections form the bonds of the lattice structure with the force-displacement relationship given in Eq. (14), for elastoplastic contact. The singum particle, or the Wigner-Seitz (WS) cell of the lattice, can be generated through Voronoi decomposition and perfectly fill the space of the lattice with a periodic pattern, so the properties of the singum particle can represent the lattice.

An example of this can be seen in Yin et al. (2023), Fig. 8(a) depicts a hexagonal packing arrangement, where a unit cell contains a central cylinder surrounded by six neighboring cylinders. To create the singum representation for the central cylinder, as shown in Fig. 8(b), the six bonds are cut by perpendicular lines to form a hexagonal shape.

Each pair of the contacting wires forms a force path through the center-center bond. The original bond length is 2R with zero force, and the deformation can be described by the stretch ratio of  $\lambda \le 1$  as the applied force increases from zero.

When the lattice is subjected to a uniform external load, the force will be transferred through the lattice by the bonds, which can be homogenized by the singum modeling (Yin 2023a; Yin and Liu 2023). The stiffness based on the current configuration can be derived by the incremental stress  $\delta\sigma_{ij}$  caused by a strain variation  $\delta\varepsilon_{kl}$  as follows:

$$\delta\sigma_{ij} = C_{ijkl}\delta\varepsilon_{kl} \tag{15}$$

where  $C_{ijkl}$  is the stiffness tensor. In linear elasticity, given an infinitesimal strain, the stress can be obtained through the stiffness

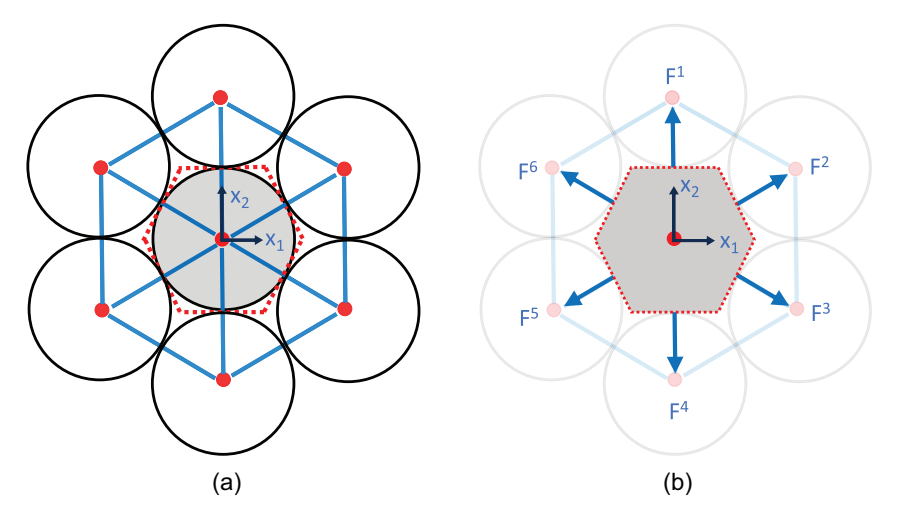


Fig. 8. Singum construction: (a) Wigner-Seitz (WS) cell in dotted lines; and (b) singum particle with point loads.

tensor. Nevertheless, because the force-interference relationship in the Hertz's model is highly non-linear, the tangential stiffness tensor at the specific spatial coordinate shall be used to accurately describe the elastic behavior (Yin 2022). When the contact between wires becomes elastoplastic, the effective mechanical behavior will be discussed in the next section.

The neighboring cylinders exert a point force represented as  $F^I$  at the position  $\mathbf{x}^I$  along each of the six edges of singum 0 shown in Fig. 4 (Yin et al. 2023). In the absence of any external body forces, this leads to the formulation of the boundary condition, ensuring equilibrium, as follows:

$$\sigma_{ij}(\mathbf{x})n_i(\mathbf{x}) = \sum_{I=1}^6 F_i^I \delta(\mathbf{x} - \mathbf{x}^I) \quad \text{for } \mathbf{x} \in \partial V_S$$
 (16)

where  $\delta(\mathbf{x})$  is the Dirac Delta function;  $\sigma_{ij}$  and  $n_i$  are the Cauchy stress tensor and surface out-normal vector of a continuum particle, respectively. The stress integral with a Singum particle  $S_{ij}$  can be written as follows (Mura 1987; Yin et al. 2023):

$$S_{ij} = \int_{Vs} \sigma_{ij}(\mathbf{x}) d\mathbf{x} = \int_{\partial V_s} x_i \sigma_{kj} n_k d\mathbf{x} = \sum_{I=1}^6 x_i^I F_j^I$$
 (17)

where  $V_s = \lambda^2 V_s^0$  is the deformed area of the singum particle with the initial area  $V_s^0 = 2\sqrt{3}(R)^2$ ; the point force  $F_i^I$  between two smooth cylinders is expressed as the derivative of the pairwise potential  $V^I$  (Yin 2022) as

$$F_i^I = \frac{\partial V^I}{\partial x_i} = \frac{V_{,\lambda}^I n_i}{2R} \tag{18}$$

where the potential function can be obtained by the elastoplastic contact model of the  $P-\lambda$  relationship in Eq. (14), which will be elaborated in the next section.

The Cauchy stress within the singum particle can be computed as the volume average of the stress integral

$$\sigma_{ij} = \frac{S_{ij}}{V} \tag{19}$$

To test the tangent stiffness of the overall structure, we apply an incremental strain variation at every point x (Yin 2023b):

$$\delta u_i(\mathbf{x}) = x_i \delta d_{ii} \tag{20}$$

where  $\delta d_{ij} = \delta u_{i,j}$  represents a linear displacement gradient tensor, which is related to the variation of the Eulerian strain at the current configuration of a stretch ratio  $\lambda$  as (Yin 2023b):

$$\delta \varepsilon_{ij} = \frac{\delta d_{ij} + \delta d_{ji}}{2\lambda^2} \tag{21}$$

The variation of Eq. (19) with the aid of Eq. (18) yields:

$$\delta\sigma_{ij} = \frac{1}{V_s} \sum_{I=1}^{6} \left( x_i^I F_{j,l}^I \delta x_l + \delta x_i^I F_j^I - x_i^I F_j^I \frac{\delta v_s}{v_s} \right)$$

$$= \frac{1}{V_s} \sum_{I=1}^{6} (x_i^I F_{j,l}^I x_k^I \delta d_{kl} + F_j^I \delta d_{ki} x_k^I - x_i^I F_j^I \delta d_{kk})$$

$$= \frac{1}{2V_s} \sum_{I=1}^{6} [(\lambda^2 V_{,\lambda\lambda}^{I0} - \lambda V_{,\lambda}^{I0}) n_i^I n_j^I n_k^I n_l^I$$

$$+ \lambda V_{\lambda}^{I0} (\delta_{ik} n_l^I n_i^I + \delta_{ik} n_l^I n_i^I - \delta_{kl} n_i^I n_i^I) [\delta d_{kl}$$
(22)

By relating the variations in the Cauchy stress and Eulerian strain with the aid of Eq. (21), the tangent stiffness tensor can be evaluated (Yin 2023a, b) as

$$C_{ijkl} = \frac{\lambda^2}{2V_s} \sum_{I=1}^{6} \left[ (\lambda^2 V_{,\lambda\lambda}^{I0} - \lambda V_{,\lambda}^{I0}) n_i^I n_j^I n_k^I n_l^I + \lambda V_{,\lambda}^{I0} (\delta_{ik} n_l^I n_i^I + \delta_{jk} n_l^I n_i^I - \delta_{kl} n_i^I n_i^I) \right]$$
(23)

where  $n_i^I = (x_i^I/|\mathbf{x}^I|)$  is the component of the unit vector from the center of a singum particle to its neighbors, and the superscript of I0 can be disregarded because each pair of the bond share the same center-center distance and thus the same derivatives of  $V_{.\lambda}$  and  $V_{.\lambda\lambda}$ .

For hexagonal packing of wire cables, the relation between stiffness tensor  ${\bf C}$  of hexagonal lattice and pairwise potential can be calculated using the identities of  $\sum_{I=1}^6 n_i^I n_j^I = 3\delta_{ij}$  and  $\sum_{I=1}^6 n_i^I n_k^I n_k^I n_l^I = \frac{3}{4} (\delta_{ij} \delta_{kl} + \delta_{ik} \delta_{jl} + \delta_{il} \delta_{jk})$  (Yin et al. 2023) as follows:

$$C_{ijkl} = \frac{\sqrt{3}}{16(R)^2} [(\lambda^2 V_{,\lambda\lambda} - 5\lambda V_{,\lambda}) \delta_{ij} \delta_{kl} + (\lambda^2 V_{,\lambda\lambda} + 3\lambda V_{,\lambda}) (\delta_{ik} \delta_{jl} + \delta_{il} \delta_{jk})]$$
(24)

where the pairwise potential  $V(\lambda)$  is obtained by the  $P-\lambda$  function.

## The Effective Elastic Constants Based on the Elastoplastic Contact

Using Eq. (14) of the  $P - \lambda$  function, the potential function can be written as

$$V(\lambda) = -2R \int_{1}^{\lambda} P(\lambda) d\lambda \tag{25}$$

which takes  $\lambda = 1$  as the reference point of the potential with V(1) = 0. Therefore, the derivatives of  $V(\lambda)$  are as follows:

$$V_{,\lambda}(\lambda) = -2RP = \begin{cases} -\frac{4\pi E^* R^2(\lambda - 1)}{W_{-1}[0.25 * e(\lambda - 1)]} & \lambda_c < \lambda \\ -9850.0 + 80.15 \times 10^6(\lambda - \lambda_c) + 11.81 \times 10^9(\lambda - \lambda_c)^2 \\ +1.196 \times 10^{12}(\lambda - \lambda_c)^3 + 47.65 \times 10^{12}(\lambda - \lambda_c)^4 & \lambda \le \lambda_c \end{cases}$$
(26)

$$V_{,\lambda\lambda}(\lambda) = -2RP_{,\lambda} = \begin{cases} -\frac{4\pi E^* R^2}{1 + W_{-1}[0.25e(\lambda - 1)]} & \lambda_c < \lambda \\ 80.15 \times 10^6 + 23.61 \times 10^9 (\lambda - \lambda_c) + 3.588 \times 10^{12} (\lambda - \lambda_c)^2 + 190.6 \times 10^{12} (\lambda - \lambda_c)^3 & \lambda \le \lambda_c \end{cases}$$

$$(27)$$

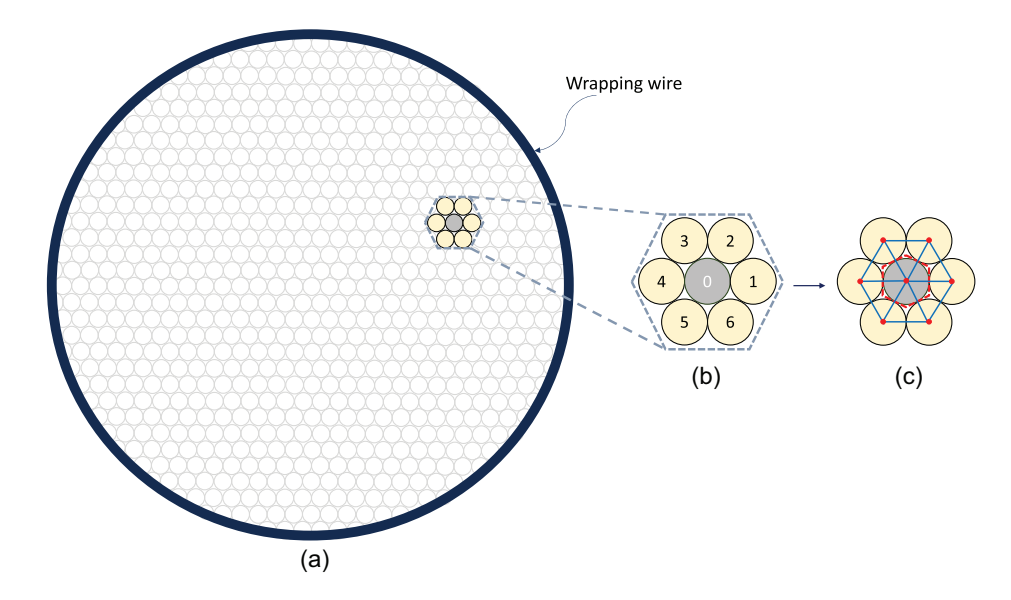


**Fig. 9.** Wire cable (a) cable cross section with wrapping wire; (b) a wire with 6 neighboring wires, and (c) Singum particle of the hexagonal prism with dotted lines.

Therefore, by substituting Eqs. (26) and (27) into Eq. (24), we can obtain the stiffness tensor in the cross-sectional plane. For example, for steel wires shown in Table 1, we can obtain when  $\lambda_c = 0.99987$  at the critical deflection,  $V_{,\lambda}(\lambda_c) = -9847.8$  J and  $V_{,\lambda\lambda}(\lambda_c) = 80.157 \times 10^6$  J. Therefore, we can obtain

$$C_{11} = \frac{\sqrt{3}}{16R^2} [3\lambda^2 V_{,\lambda\lambda} + \lambda V_{,\lambda}] = 41.638 \text{ GPa}$$

$$C_{12} = \frac{\sqrt{3}}{16R^2} [\lambda^2 V_{,\lambda\lambda} - 5\lambda V_{,\lambda}] = 13.888 \text{ GPa}$$

$$C_{66} = \frac{\sqrt{3}}{16R^2} [\lambda^2 V_{,\lambda\lambda} + 3\lambda V_{,\lambda}] = 13.875 \text{ GPa}$$
(28)

where  $C_{66} = (C_{11} - C_{12})/2$ .

Substituting the preceding equation into Eq. (4), we can obtain

$$C_{13}=16.658~{\rm GPa};~~C_{33}=191.37~{\rm GPa};~~C_{44}=69.762~{\rm GPa}$$
 (29)

For different values of  $\lambda$ , the transversely isotropic stiffness tensor of the cable will be different so that we can use the prestress to tailor the effective stiffness of the cable.

To produce prestress in the cross section and control  $\lambda$ , bands encircling the wire cable are used to exert wrapping forces upon the wires. The bands are assumed to produce a uniform transverse compression in the cable. A wire cable with a wrapping band around it is shown in Fig. 9(a). For each inner wire, there exist six neighboring wires in Fig. 9(b) so that the wire can be represented by a hexagonal prism in Fig. 9(c).

Notice that this is an ideal situation where the force is uniformly transferred through the lattice by the center-center normal force. When friction or lattice defects occur in an actual situation, the force transfer may be slightly different. However, this paper focuses on the ideal situation with a periodic force and displacement distribution in the hexagonal lattice, which can be homogenized into a transversely isotropic solid.

When a wrapping force denoted as F is applied in the unit length of a band, it leads to a contact force P between the cylinders and a change of the center-center distance in the wire cable. The change

in radius, which is expressed as  $\lambda$ , will reduce from its initial value of 1 at the zero wrapping force condition. Consequently, by expressing the stiffness tensor C in terms of  $\lambda$ , we can establish a connection between the elastic modulus and the wrapping force.

Given the force in the band of homogenized cable with the radius  $R_d$  in Fig. 10, the force produces a hydrostatic pressure  $\sigma_m$  in the cross section, which is related to the hoop stress  $\sigma_h$  as

$$\sigma_h = \frac{\sigma_m R_d}{t_h} \tag{30}$$

where  $t_h$  = thickness of a band. The wrapping force F can be computed as

$$F = \sigma_h t_h = \sigma_m R_d \tag{31}$$

The hydrostatic pressure  $\sigma_m$  and the contact force P at each wire contact point can be computed through the Singum model through Eqs. (17) and (19) as follows:

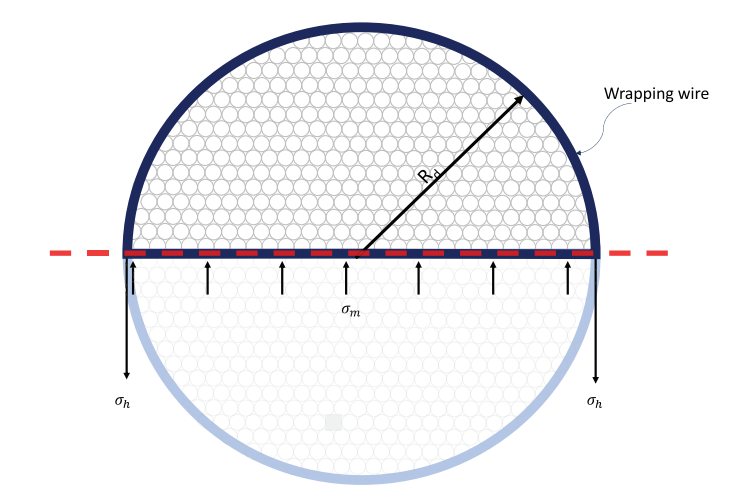


Fig. 10. Wire cables compressed by a wrapping band.

$$V_{s}\sigma_{m}\delta_{ij} = \sum_{I=1}^{6} x_{i}^{I}F_{j}^{I} = PR\lambda \sum_{I=1}^{6} n_{i}^{I}n_{j}^{I}$$
 (32)

Using the identity of  $\sum_{I=1}^{6} n_i^I n_i^I = 3\delta_{ij}$ , we obtain

$$\sigma_m = \frac{3PR\lambda}{V_s}$$
 or  $P = \frac{V_s\sigma_m}{3R\lambda} = \frac{V_sF}{3RR_d\lambda}$  (33)

Given a wrapping force F, substituting P of Eq. (33) into Eq. (14), we can calculate  $\lambda$ , which will be used to determine the effective stiffness tensor in Eq. (24). Therefore, we can inversely control the stiffness in the cross section by tailoring the wrapping force.

#### **Results and Discussion**

As Singum modeling of the effective stiffness of packed cables with wrapping forces has been validated by the experiments and verified by the FEM analysis, we can use it to predict the mechanical behavior of the cable and analyze the stress transfer when the cable is subjected to a single wire breakage.

When the wire is still in the linear elastic range, Hertz's model provides a nonlinear  $P-\lambda$  curve in Fig. 3, and the Singum model transfers the forces to stresses, which further increases the nonlinearity of the effective elasticity. When the wrapping force is higher than  $P_c$ , the elastoplastic contact behavior leads to a lower effective stiffness of the cable in the cross section.

For a homogenized cylinder with properties listed in Table 1, the stiffness constants can be calculated using Eqs. (28) and (4), and the results are shown in Fig. 11. The increasing trend indicates that

the stiffness of tightly packed cylindrical steel wires can be influenced and adjusted by varying the magnitude of the wrapping force, consequently, the ratio  $\lambda$ . There is a sudden and substantial spike in the stiffness constants for a minimal  $\lambda$ , particularly in comparison to the initial loose configuration where no wrapping force is applied and  $\lambda=1$ . This phenomenon underscores the substantial impact that adjusting the wrapping force can have on enhancing the overall stiffness of wire cables. Note that bridge cables typically use high strength steel wire with a high yield strength at 1.2–1.5 GPa, so that the stiffness can exhibit a much higher range changing with the wrapping force.

In Fig. 11(a), the effective stiffness of the packed wire cable increases in the elastic stage until the yield point and shows a gradual decrease once yielding initiates. This is different from the elastic perfectly plastic bulk material, which exhibits a constant stiffness in the elastic range and a zero stiffness after yielding. For the cable, the transition from the elastic range to the plastic stage is marked by the sudden drop of the stiffness constants at the critical  $\lambda$ , as shown in Figs. 11(b and c).

In order to demonstrate the effect of wrapping force on the effective stiffness of a cable, we use the low-carbon steel wires with material constants given in Tables 1 and 2 with a diameter of 5mm. Approximately 36,275 wires are required to assemble a cable with a diameter of 1m. The wrapping force F changing with  $\lambda$  is shown in Fig. 12(a).

Using the relationship between the stiffness tensor and  $\lambda$ , we can obtain the stiffness tensor changing with the wrapping force F in Fig. 12(b). When  $F \ge F_c = 3.412$  MN/m,  $P_c = 197.0$  kN/m is reached, and the elastoplastic contact is applied. Different from the elastic perfectly plastic bulk material, when the wrapping force reaches  $F_c$ , the material can still sustain a much higher wrapping

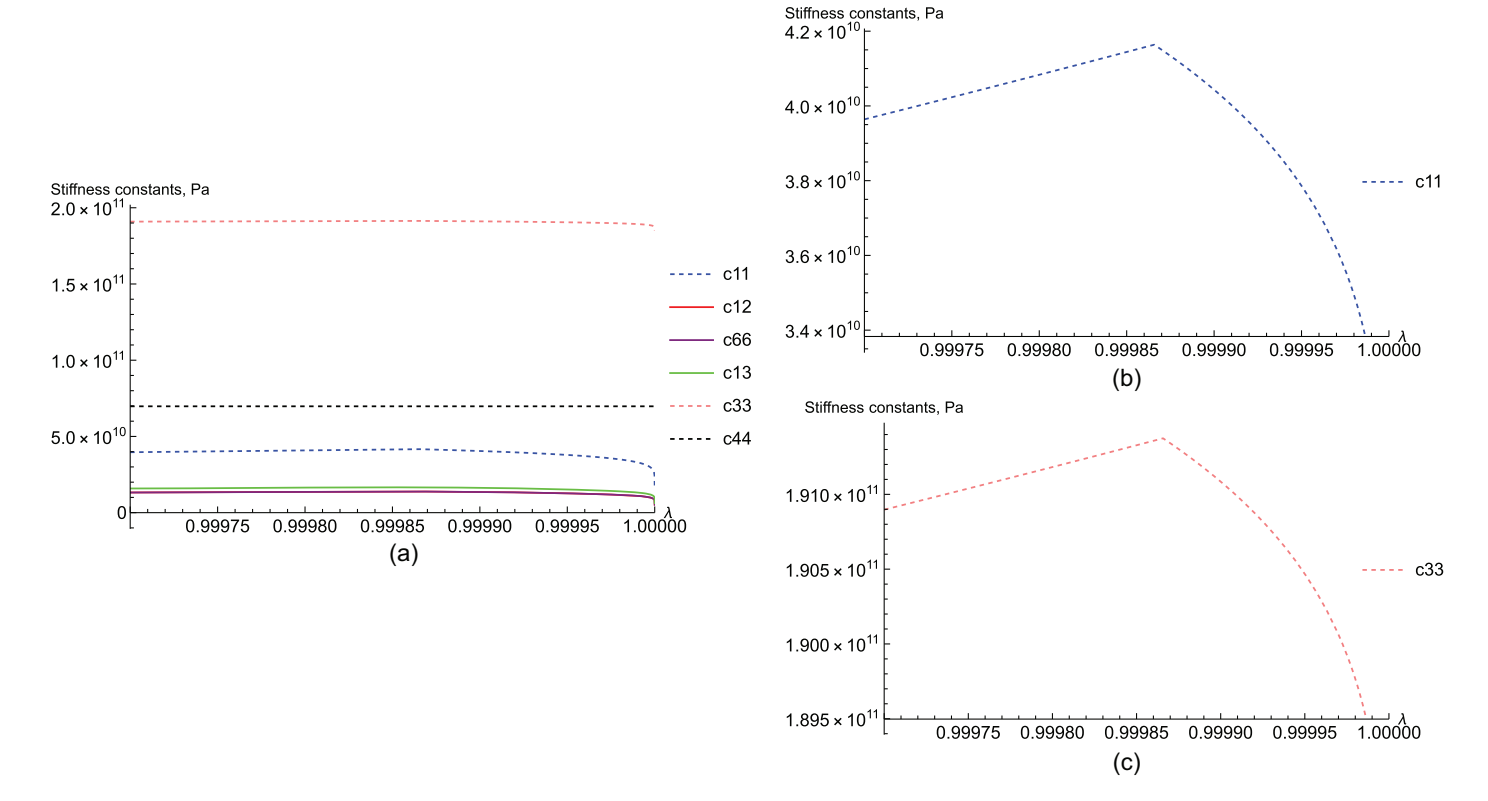


Fig. 11. Stiffness constants varying with  $\lambda$  for a low-carbon steel cable: (a)  $\lambda \in (0.992, 1)$ ; (b)  $C_{11}$  for  $\lambda \in (0.9997, 1)$ ; and (c)  $C_{33}$  for  $\lambda \in (0.9997, 1)$ .

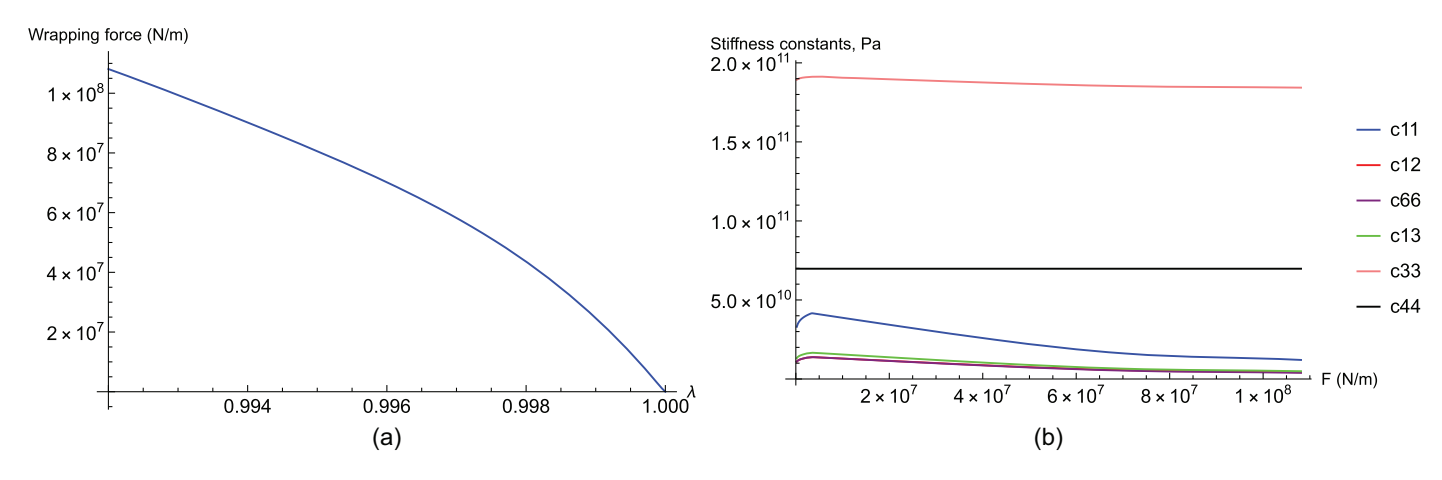


Fig. 12. Effect of wrapping force on wire cables: (a) wrapping force varying with  $\lambda$ ; and (b) stiffness constants varying with Wrapping force.

force, which leads to the growth of the plastic zone in a wire from one point to a larger area, which is not favorable in actual application due to the permanent deformation and the loss of stiffness shown in Fig. 12(b).

Note that the validation of the formulation requires many wires to calculate the average stress and strain with precise control of the loading conditions for a uniform loading transfer. As a qualitative demonstration, a 61-wire cable has been set up in the laboratory with a wrapping band for compressive testing, which is documented in the Supplemental Materials. Although it is not sufficient to provide a quantitative relationship between the effective stiffness and the prestress in the experiments, it clearly shows the effective stiffness in the cross section increases with tightening of the band or increasing the prestress.

When the cable is subjected to an additional axial tension, due to the effect of Poisson's ratio, the radius of wire R reduces, which causes the redefinition of  $\lambda$  and the change of prestress. Therefore, the effective stiffness in the cross section will change with the axial loading as well. Because the size of bands cannot be changed frequently, additional axial tension will lead to the decrease of the wrapping force and, thus, lower the stiffness in the cross section, which can be predicted by the present model. In general, the cable is under infinitesimal elastic deformation, and the effect of Poisson's ratio on wrapping force shall be minimal. Alternatively, the temperature change may also change the wrapping force, and the method in the recent paper (Liu and Yin 2023) can be used to analyze the thermoelastic behavior. A detailed analysis of bridge cables is underway.

## Conclusions

This study introduces the singum model as a novel approach for analyzing the mechanical properties of packed wire cables featuring cylindrical steel wires arranged in a two-dimensional hexagonal lattice structure tightened by wrapping bands at a certain interval. Within this framework, the behavior of an inner cylinder is replicated using a continuous singum particle, while the interaction forces between cylinders adhere to the Hertz contact model. An elasto-plastic contact model for two cylinders is formulated, and an empirical formula is provided by curve fitting the FEM results. This formulation enables the determination of the effective constitutive relationship for the cross section of wire cables. Significantly, variations in displacement result in configurational forces due to

wrapping, leading to a substantial modification in the effective stiffness of the packed cylinders. This research investigates the effective transverse stiffness of packed wire cables, employing the singum model, FEM, and experimental tests. The impact of wrapping force on effective transverse stiffness is illustrated, and experiments are conducted to validate the model's potential function. The comparison with experimental results highlights the model's capability. However, it is crucial to acknowledge some limitations: the empirical formula derived from curve fitting is based on low-carbon steel wires and assumes an elastic and perfectly plastic behavior. In addition, the assumption of uniform compression induced by the wrapping bands represents an idealized scenario. In reality, factors such as friction or lattice defects may lead to variations in force transfer within the cable structure.

# Appendix I. Experimental Testing of the Cylinderical Contact

Experimental tests were conducted at the Carleton Laboratory, Columbia University, to investigate the elastoplastic contact parameters of cylinders in contact. In the experiment, only one cylinder is used, and it is sandwiched in between two hardened steel platens; these steel platens can be considered to be rigid Surfaces and, with mirror symmetry, can reproduce the deformation pattern of the contact of two identical cylinders. The experimental setup is shown in Fig. 13.

A universal testing machine (Instron 600DX UTM) with a maximum capacity of 135 kips (600 kN) was used to apply a compression load, and the load-displacement ( $P-\delta$ ) relationship was identified.

Three different samples of Low carbon cylinders of diameter 50 mm (1.92") and length 100.7 mm (4") were tested, and the material properties are seen in the Table 1. The hardened steel plates are  $15.24 \times 15.24$  cm (6"  $\times$  6") plates with a thickness of 2.54 cm (1") and a yield strength of 1,379 MPa (200,000 psi). The specimens were laid in the horizontal direction and held in place using steel plates that were oiled to prevent friction, as shown in Fig. 10. The specimens were loaded uniaxially using a displacement control of 0.254 mm/min. The time, load, and deflection values for all tests were recorded through a data acquisition system.

To determine the displacement of the specimen only, machine compliance (deformations associated with the load frame, load cell,



Fig. 13. Experimental setup for cylindrical contacting compression test

and grips) must be removed from this measurement. When a test's total displacement is small, machine compliance can be a significant portion of the output displacement given by the software. Accordingly, the values from the experimental test were corrected by conducting a compliance test. The results obtained from the experimental test are shown in Fig. 3. Note that when the load is higher than the yielding limit, the experimental results of the force versus the interference does not follow Fig. 7 due to our assumption of elastic perfectly plastic materials, and further investigation is still needed to release the elastic perfectly plastic assumption of the wire under compression.

# Appendix II. Derivation of the Critical Contact Load and Interference

A short summary of Green (2005)'s analysis for critical contact and interference is provided as follows. For a load per unit length, P, maximum Hertzian pressure  $p_0$  and the half-width b is given by

$$p_0 = \frac{2P}{\pi b} \tag{34}$$

$$b = \sqrt{\frac{2PR}{\pi E^*}} \tag{35}$$

Note that here the radius R of two cylinders is only the twice "R" that Green (2005) used with the same symbol of R. Therefore, the formulation will exhibit a difference of this coefficient of 2.

Assuming that the  $x_1$ -axis aligns with the contact line, the  $x_2$ -axis is tangent to both cylinders, and the  $x_3$ -axis corresponds to the loading direction, the stress under the contact at  $\zeta = |x_3/b|$  is given by

$$\sigma_3 = -\frac{p_0}{\sqrt{1+\zeta^2}}\tag{36}$$

$$\sigma_2 = p_0 \left( \left( 2\zeta - \sqrt{1 + \zeta^2} \right) \left( 2 - \frac{1}{1 + \zeta^2} \right) \right)$$
 (37)

For plane strain the transverse stress is given by

$$\sigma_1 = \nu(\sigma_z + \sigma_y) = 2\left(\zeta - \sqrt{1 + \zeta^2}\right)\nu p_0 \tag{38}$$

The von Mises stress,  $\sigma_e$ , is given by

$$\frac{\sigma_e}{p_0} = \sqrt{\frac{\left[1 - 2\zeta\left(\sqrt{1 + \zeta^2} - \zeta\right)\right]\left[1 + 4\zeta^2 - 4(1 + \zeta^2)(1 - \nu)\nu\right]}{1 + \zeta^2}}$$
(39)

which is not necessarily maximized at  $\zeta=0$ . From the equation, it can be seen that the maximum von Mises stress varies with  $\zeta$ , Hence, the maximum von Mises stress is obtained from taking the derivative of the von Mises stress as  $(d\sigma_c/d\zeta)=0$ . Using the von Mises theory to predict yielding onset, we can derive the critical values for force per unit length, interference, and half-width as

$$P_c = \frac{\pi R (C\sigma_y)^2}{2E^*} \tag{40}$$

$$b_c = \frac{Rc\sigma_y}{E^*} \tag{41}$$

$$\delta_c = \frac{R}{2} \left( \frac{C\sigma_y}{E^*} \right)^2 \left( 2 \ln \frac{4E^*}{C\sigma_y} - 1 \right) \tag{42}$$

where constant C is defined as  $C = (p_0/\sigma_y)$  with the maximum value of  $\sigma_e$  at the yield stress, which is explicitly written as

$$C = \begin{cases} \frac{1}{\sqrt{1 + 4(\nu - 1)\nu}} & \nu \le 0.1938\\ 1.164 + 2.975\nu - 2.906\nu^2 & \nu > 0.1938 \end{cases}$$
(43)

where  $\nu$  is the Poisson's ratio.

Note that  $\delta_c$  exhibits a minor difference from Green (2005) in terms of " $4E^*$ " instead of "2E'." For the wire given in Table 1, we can obtain C=1.795,  $P_c=197.0$  kN/m,  $\delta_c=6.713\times10^{-6}$  m,  $\lambda_c=0.99987$  for the plane strain case, which has been verified by the FEM results.

#### **Data Availability Statement**

All data, models, or code that support the findings of this study are available from the corresponding author upon reasonable request.

#### **Acknowledgments**

The authors thank Dr. Steve "Seonghyeok" Song for the fruitful discussion about the bridge cable inspection and repair. This work is sponsored by the National Science Foundation IIP No. 1738802, IIP No. 1941244, CMMI No. 1762891, and US Department of Agriculture NIFA #2021-67021-34201, whose support is gratefully acknowledged. We thank Dr. Liming Li, Dr. Will Hunnicutt, and Mr. James Basirico for their help with the experiments.

#### **Supplemental Materials**

The Supplemental Materials package is available online in the ASCE Library (www.ascelibrary.org).

#### References

- Brügger, A., S.-Y. Lee, J. Robinson, M. Morgantini, R. Betti, and I. Noyan. 2022. "Internal contact mechanics of 61-wire cable strands." *Exp. Mech.* 62 (8): 1475–1488. https://doi.org/10.1007/s11340-022-00896-w.
- Chacar, J.-P. M. 2001. "Design of cable systems for cable suspension bridges." Ph.D. thesis, Dept. of Civil and Environmental Engineering, Massachusetts Institute of Technology.
- Cinar, A., and G. Sinclair. 1986. "Quasi-static normal indentation of an elasto-plastic half-space by a rigid circular cylinder of infinite length." *Int. J. Solids Struct.* 22 (8): 919–934. https://doi.org/10.1016/0020 -7683(86)90071-5.
- Dumas, G., and C. Baronet. 1971. "Elastoplastic indentation of a half-space by an infinitely long rigid circular cylinder." *Int. J. Mech. Sci.* 13 (6): 519–530. https://doi.org/10.1016/0020-7403(71)90039-7.
- Ghaednia, H., S. A. Pope, R. L. Jackson, and D. B. Marghitu. 2016. "A comprehensive study of the elasto-plastic contact of a sphere and a flat." *Tribol. Int.* 93 (Part A): 78–90. https://doi.org/10.1016/j.triboint .2015.09.005.
- Ghaednia, H., X. Wang, S. Saha, Y. Xu, A. Sharma, and R. L. Jackson. 2017. "A review of elastic–plastic contact mechanics." Appl. Mech. Rev. 69 (6): 060804. https://doi.org/10.1115/1.4038187.
- Gjelsvik, A. 1991. "Development length for single wire in suspension bridge cable." J. Struct. Eng. 117 (4): 1189–1200. https://doi.org/10 .1061/(ASCE)0733-9445(1991)117:4(1189).
- Goldsmith, W. 1999. The theory and physical behaviour of colliding solids. Mineola, NY: Dover Publications.
- Green, I. 2005. "Poisson ratio effects and critical valus in spherical and cylindrical hertzian contacts." Appl. Mech. Eng. 10 (3): 451.
- Griffin, K. 1961. "Impact: The theory and physical behaviour of colliding solids. w. goldsmith. Arnold, London. 1960. 379 pp. Diagrams. 90s." Aeronaut. J. 65 (606): 443. https://doi.org/10.1017/S036839310 0074861.
- Guo, T., X. Hua, Z. Yan, and C. Bai. 2020. "Research on the elastic–plastic external contact mechanical properties of cylinder." Sci. Prog. 103 (2): 0036850420927817. https://doi.org/10.1177/0036850420927817.
- Guo, T., R. Ji, Y. Ma, and L. Peng. 2022. "Tangential elastic contact model of the cylindrical contact with different axis crossing angles." *Sci. Prog.* 105 (2): 003685042210941. https://doi.org/10.1177/00368 504221094183.
- Hertz, H. 1882. "Uber die beruhrung fester elastischer korper und uber die harte." Crll 1882 (92): 156–171. https://doi.org/10.1515/crll.1882.92 .156.
- Jackson, R. L., and I. Green. 2005. "A finite element study of elasto-plastic hemispherical contact against a rigid flat." J. Trib. 127 (2): 343–354. https://doi.org/10.1115/1.1866166.
- Johnson, K. L. 1987. Contact mechanics. Cambridge, UK: Cambridge University Press.
- Kogut, L., and I. Etsion. 2002. "Elastic-plastic contact analysis of a sphere and a rigid flat." J. Appl. Mech. 69 (5): 657–662. https://doi.org/10.1115 /1.1490373.

- Komvopoulos, K. 1989. "Elastic-plastic finite element analysis of indented layered media." J. Tribol 111 (3): 430–439. https://doi.org/10.1115/1 .3261943.
- Lankarani, H. M., and P. Nikravesh. 1989. "A contact force model with hysteresis damping for impact analysis of multibody systems." In Vol. 3691 of Proc., Int. Design Engineering Technical Conf. and Computers and Information in Engineering Conf., 45–51. Reston, VA: ASCE.
- Lankarani, H. M., and P. E. Nikravesh. 1994. "Continuous contact force models for impact analysis in multibody systems." *Nonlinear Dyn.* 5 (2): 193–207. https://doi.org/10.1007/BF00045676.
- Liu, C., and H. Yin. 2023. "Tailorable thermoelasticity of cubic lattice-based cellular and granular materials by prestress." *Mater. Des.* 233 (Dec): 112223. https://doi.org/10.1016/j.matdes.2023.112223.
- Montoya, A., H. Waisman, and R. Betti. 2012. "A simplified contact-friction methodology for modeling wire breaks in parallel wire strands." *Comput. Struct.* 100-101 (Jun): 39–53. https://doi.org/10.1016/j.compstruc.2012.03.003.
- Mura, T. 1987. Vol. 3 of Micromechanics of defects in solids. Dordrecht, Netherlands: Springer.
- Olsson, E., and P.-L. Larsson. 2016. "A unified model for the contact behaviour between equal and dissimilar elastic-plastic spherical bodies." *Int. J. Solids Struct.* 81 (Mar): 23–32. https://doi.org/10 .1016/j.ijsolstr.2015.10.004.
- Radzimovsky, E. I. 1953. Stress distribution and strength condition of two rolling cylinders pressed together: Engineering experiment station. Bulletin; no. 408. Urbana, IL: Univ. of Illinois Urbana-Champaign.
- Raoof, M., and Y. P. Huang. 1992. "Wire recovery length in suspension bridge cable." *J. Struct. Eng.* 118 (12): 3255–3267. https://doi.org/10.1061/(ASCE)0733-9445(1992)118:12(3255).
- Sharma, A., and R. L. Jackson. 2017. "A finite element study of an elastoplastic disk or cylindrical contact against a rigid flat in plane stress with bilinear hardening." *Tribol. Lett.* 65 (3): 1–12. https://doi.org/10.1007/s11249-017-0894-9.
- Sugunesh, A., and A. J. Mertens. 2021. "2d fea study of hertzian contact stress between two cylindrical bodies." *Mater. Today Proc.* 44 (Jan): 4474–4478. https://doi.org/10.1016/j.matpr.2020.10.721.
- Tabor, D. 2000. The hardness of metals. Oxford, UK: Oxford University Press.
- Yin, H. 2022. "A simplified continuum particle model bridging interatomic potentials and elasticity of solids." *J. Eng. Mech.* 148 (5): 04022017. https://doi.org/10.1061/(ASCE)EM.1943-7889.0002096.
- Yin, H. 2023a. "Generalization of the singum model for the elasticity prediction of lattice metamaterials and composites." *J. Eng. Mech.* 149 (5): 04023023. https://doi.org/10.1061/(ASCE)EM.1943-7889.0002152.
- Yin, H. 2023b. "Improved singum model based on finite deformation of crystals with the thermodynamic equation of state." *J. Eng. Mech.* 149 (4): 04023018. https://doi.org/10.1061/JENMDT.EMENG-6831.
- Yin, H., J. Cui, L. G. Teka, and M. Zadshir. 2023. "Effect of wrapping force on the effective elastic behavior of packed cylinders." *J. Appl. Mech.* 90 (3): 031003. https://doi.org/10.1115/1.4056212.
- Yin, H., and C. Liu. 2023. "Anisotropy and asymmetry of the elastic tensor of lattice materials." *J. Elast.* 154 (5): 659–691. https://doi.org/10.1007/s10659-023-10028-7.
- Yin, H., and Y. Zhao. 2016. *Introduction to the micromechanics of composite materials*. Boca Raton, FL: CRC Press.
- Zhang, W., J. Chen, C. Wang, D. Liu, and L. Zhu. 2022. "Research on elastic-plastic contact behavior of hemisphere flattened by a rigid flat." *Materials* 15 (13): 4527. https://doi.org/10.3390/ma15134527.